Detailed Numerical Simulation for Optimization of Radiation Efficiency of Porous Burners

C. Wieland[1*], P. Weinbrecht[2], C. Weis[2], P. Habisreuther[3] and D. Trimis[2]

*Christoph.Wieland@partner.kit.edu

[1] *DVGW Research Centre at the Engler-Bunte-Institute of the Karlsruhe Institute of Technology, Engler-Bunte-Ring 1-9, 76131 Karlsruhe, Germany*

[2] *Engler-Bunte-Institute, Karlsruhe Institute of Technology, Engler-Bunte-Ring 1-7, 76131 Karlsruhe, Deutschland*

[3] *Institute for Technical Chemistry, Karlsruhe Institute of Technology, Hermann-von-Helmholtz-Platz 1, 76344 Eggenstein-Leopoldshafen, Deutschland*

Abstract

In porous burners, premixed combustion of gaseous fuels inside the cavities of an open-pore ceramic matrix heats the solid material to temperatures of 1400 °C, which leads to the emission of electromagnetic radiation with its intensity maximum at infrared light. The net thermal radiation emission can be used for efficient, fast and uniform heat transfer in various technical applications. Improving radiation efficiency correlates to increasing thermal radiation flux at constant thermal power, implicating a potential for reduction of fuel consumption and associated emissions for a given application. Additive manufacturing techniques offer new opportunities in the design of ceramic structures. However, the design of an optimized structure requires detailed knowledge of processes and conditions inside the porous matrix during operation, the experimental determination of which is complex and challenging. Inside the porous burner, chemical combustion reactions coincide with complex interaction between thermo-physical transport processes that occur within solid and gaseous phase, and across phase boundary. Flow, heat release and resulting heat flows influence each other. The numerical model used in this work considers gaseous and solid phases, includes flow, enthalpy transport, conjugate heat transfer, radiative heat transfer between solid surfaces as well as combustion kinetics according to a skeletal chemical reaction mechanism. These phenomena are resolved on the pore scale in three-dimensional space (Direct Pore Level Simulation, DPLS). The calculations are performed based on the finite volume method using standard applications implemented in the OpenFOAM library. The reactive flow and enthalpy field are calculated for a lateral periodical representative element of flat two-layer porous burner in full axial extension of flame trap and porous structure. The present study presents simulations of three different structures, each at four settings of specific thermal power. Results indicate that specific surface area of the porous structure is a major influencing parameter for increasing radiation efficiency, whereas no correlation of the orientation of an anisotropic structure on radiation efficiency was observed.

Introduction

A radiant porous burner is constructed as a two-layer system, consisting of a flame trap and the structure of an open-pore solid in which combustion takes place. The flame trap is made of mullite fibre, a ceramic material with low thermal conductivity. The unburned premixed air-fuel mixture passes the flame trap through a pattern of straight circular ducts. The porous structure is made of silicon-infiltrated silicon carbide (Si-SiC), a ceramic composite material resistant to thermal and mechanical stresses in an oxidative high temperature environment [1]. Heat release associated with the combustion reaction within the cavities of the Si-SiC heats the porous structure to temperature in the order of the gas temperature. At this high temperature, the solid material emits intensive thermal radiation. The upstream mullite layer serves as a flame barrier by a gas velocity exceeding the flame speed and thermal quenching in the ducts. With its low thermal conductivity, the mullite layer also represents a thermal barrier between the downstream high temperature combustion zone and an upstream mixing and gas distribution zone.

For the manufacturing of Si-SiC structures, a replica technology is available that uses additive manufactured polymeric precursors [2]. This technology offers a wide range of design opportunities that can be exploited for the optimization of the radiant burner. An optimization process requires detailed

knowledge of the processes and conditions occurring inside the radiant porous burner. However, phenomena of heat release and transport as well as resulting heat fluxes and temperature fields within the porous structure are interrelated and experimentally accessible to a limited extent. Stelzner et al. determined the flame position by detecting the hydroxyl radical (OH) using laser induced fluorescence in the gap of a sliced porous structure [3]. Dunmon et al. resolved the flame structure of porous media combustion by investigation of gas density through detection of krypton attenuation with x-ray computer tomography [4]. Detailed numerical simulation of processes resolved on pore scale inside porous burners require significant computational effort. Bedoya et al. simulated combustion of methane (CH_4) in porous media in 3D DPLS employing a single step chemical reaction mechanism and neglecting radiation [5]. Yakovlev et al. performed 3D DPLS of CH_4 combustion in a packed bed, employing a detailed chemical reaction mechanism and considering radiation in a view-factor model [6].

The present study focusses on radiation output of two-layered porous burners. 3D DPLS of radiant porous burners, employing a skeletal chemical reaction mechanism and a finite volume discrete ordinate method (fvDOM) are used to examine three different regular porous structures at different loads of specific thermal power. Integral radiation efficiency is determined, load dependency of internal fields and structure dependency of the gas-solid interface fluxes are investigated.

Simulation Setup

Simulation domains in the present study consider both layers of the radiant burner, flame trap and porous structure. In main flow direction (axial direction), flame trap and porous structure are fully resolved; in lateral directions, the simulation domain covers a representative element that allows for application of periodic boundary conditions. The porous structures considered in the present study are composed as stacks of two different periodic unit cells, namely the Kelvin Cell (KC) and the Rotated Cube (RC) [7]. The KC setup uses three KC unit cells, forming a porous structure with extensions of 6 mm in lateral directions and 18 mm in axial direction. The RC unit cell is used in two different orientations, a ‘dense’ (RC-D) configuration with high optical blockage in axial direction and a ‘light’ (RC-L) configuration with low optical blockage in axial direction. RC-D setup with two unit cells in axial direction results in 22.5 mm structure height; three RC unit cells in light orientation are corresponding to 19.5 mm structure height for RC-L setup. The flame trap is a block of 20 mm thickness with a pattern of parallel circular ducts of 1 mm diameter; the pattern is tailored to each porous structure for application of periodic boundary conditions. Figure 1 gives illustrations of flame trap and porous structure for all three geometry setups.

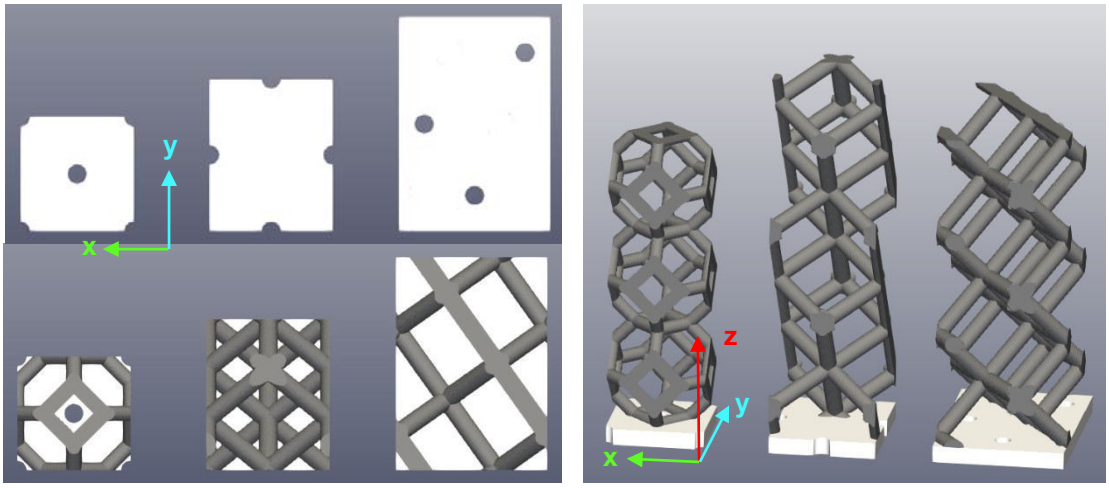

Figure 1. Flame trap and porous structure left to right: KC, RC-D, RC-L. Top left: flame trap duct pattern; bottom left: axial view on porous structures; right: 3D-view on structures.

All three setups have a structure porosity of 90 %. RC-D and RC-L are built from the same unit cell; thus, these structures show the same specific surface area of 362 m^{-1} (365 m^{-1}), while the KC setup shows a higher value of 471 m^{-1}.

The computational mesh comprises three separate regions and was generated with the SnappyHexMesh utility of the OpenFOAM library. Typical cell size is < 300 µm for the flame trap

region and < 55 µm for regions of both porous structure and gas phase. The resulting mesh sizes are given amongst other parameters in Table 1. Both, flame trap and porous structure are considered as solid region with heat conductivity modelled as a function of temperature according to their respective datasheet [8,9]. The gas phase is considered as laminar flow of a reactive multi component mixture using the OpenFOAM standard finite rate chemistry model employing a skeletal chemical reaction mechanism that considers 17 species [10]. Radiative transport of heat through the gas region is considered by fvDOM with 3 x 6 discretization, resulting in 72 discrete ordinates; interaction of the gas phase with radiative transfer is neglected and surfaces are considered as grey with an emissivity of 0.9 and 0.3 for the porous structure and the flame trap, respectively. The regions are thermally coupled by equalized interface temperature and heat flux normal to the interface; steady state is being applied for solid regions while gas phase transient calculations are carried out using the chtMuliRegionFoam solver of the OpenFOAM library. Periodic boundary conditions are applied in lateral directions, directly coupling the computational domain boundary to its translational neighbour boundary. With this boundary condition, the simulation can be considered as a repetitive element of an infinite extended burner plate. At the inlet, temperature is set to a fixed value of 300 K for both, gas and solid region. Gas composition represents premixed CH_4 and air at an equivalence ratio $\phi = 0.91$ resulting in an adiabatic flame temperature of 2147 K. The fixed value of inlet gas velocity is varied between different simulations, resulting in different specific thermal power settings. At the outlet of the computational domain, gas temperature T_G is calculated with the Neumann boundary condition $\partial T_G / \partial \vec{n} = 0$ and radiation temperature is set to 300 K with outlet emissivity of 1.0.

Table 1. Geometric information on setups for detailed simulations.

	Cells in Domain	Domain Dimensions			Porous Structure	Structure Porosity	Specific Surface Area
		Δx	Δy	Δz	Δz	e	S_V
	-	mm	mm	mm	mm	-	m^{-1}
KC	$6.8 \cdot 10^6$	6.0	6.0	44.0	18.0	90.0 %	471
RC-D	$5.1 \cdot 10^6$	6.5	8.0	46.5	22.5	90.3 %	362
RC-L	$7.8 \cdot 10^6$	8.0	11.3	43.5	19.5	90.4 %	365

Results and Discussion

For each of the three setups KC, RC-D and RC-L, four different simulations have been conducted with inlet velocity in the range between 3 m/s and 12 m/s. Specific thermal power P_A that is calculated from inlet values of velocity u, gas density ρ, mass fraction of fuel y_f, gas phase area A_f, the fuel's lower heating value LHV and lateral domain dimensions Δx and Δy according to Eq. (1), ranges from 360 kW/m² to 900 kW/m².

$$P_A = \frac{(u\, A_f\, \rho\, y_f)_{inlet} \cdot LHV}{\Delta x \cdot \Delta y} \tag{1}$$

Radiation efficiency η_{rad} is defined as fraction of the specific thermal power that is emitted as radiative heat to the ambient. For the present simulations, η_{rad} is calculated according to Eq. (2) as the ratio of area averaged radiative flux $\bar{q}_r$ at the outlet boundary and P_A.

$$\eta_{rad} = \frac{\bar{q}_r}{P_A} = \frac{\int q_r dA_{out}}{P_A \cdot \Delta x \cdot \Delta y} \tag{2}$$

Based on the simplified model of radiative heat transfer between two parallel walls of fixed temperature, $\bar{q}_r$ is also used to derive an effective radiation temperature T_{rad}^{eff} as function of the Stefan-Boltzmann constant $\sigma_{SB} = 5.67 \cdot 10^{-8}\ W/(m^2 \cdot K^4)$, outlet boundary radiation temperature $T_{rad}^{out} = 300\ K$ and emissivity of porous structure $\epsilon_{por} = 0.9$

$$T_{rad}^{eff} = \left(\frac{\bar{q}_r}{\sigma_{SB} \cdot \epsilon_{por}} + (T_{rad}^{out})^4 \right)^{\frac{1}{4}} \tag{3}$$

Both, radiation efficiency and effective radiation temperature are shown in Figure 2 for all simulated cases as a function of specific thermal power. For all structure setups, radiation efficiency decreases with increasing thermal power. For the KC setup, radiation efficiency ranges from 53.3 % to 32.1 %, while values for the RC setups range from 49.5 % to 30.7 %. Decreasing radiation efficiency indicates that a reduced share of the energy released by combustion reaction is transferred into radiative heat; as a consequence, the outlet gas temperature increases with increasing specific thermal power in the present study. Despite their difference in structure orientation, both RC setups show the same radiation efficiency for each thermal power setting.

In contrast to the radiation efficiency η_{rad}, the effective radiation temperature T_{rad}^{eff} increases with increasing thermal power, indicating that structure temperature and radiative flux increase with increasing thermal power. Again, values for RC-D and RC-L are the same and they are lower than the respective values for the KC setup.

Equal values in radiation efficiency and effective radiation temperature for both RC setups indicate that structure orientation does not show an influence on the net heat flux. Moreover, results indicate a correlation between specific surface area and radiation efficiency.

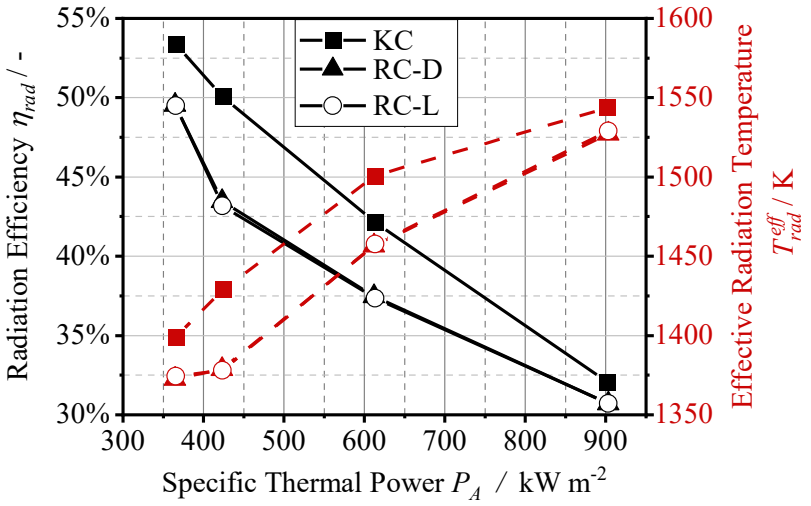

Figure 2. Radiation efficiency (solid lines) and effective radiation temperature (dashed lines) of the simulated cases depending on the specific thermal power

In order to compare the simulated cases amongst each other, the three-dimensional data are transformed into one-dimensional plots along the main flow axis *z*, which are presented in Figure 3. For generation of these plots, cell values of the computational domain are evaluated on 100 equidistant two-dimensional slices that are oriented perpendicular to the main flow direction. For each slice, solid and gaseous region are evaluated separately with solid temperature T_S (red lines) as area weighted average value of the slice and both gas temperature T_G (black lines) and hydroxyl radical (OH) mass fraction (blue lines) as values averaged by the absolute value of the axial mass flow rate. Different line styles in Figure 3 denote varying specific thermal power settings. Negative values on the horizontal axis denote the flame trap related part of the domain, positive values refer to the section including the porous structure and additional space volume. The additional space separates the porous structure from the outlet boundary; thus, values related to the gas phase cover an increased range of axial coordinates.

For all cases, flame trap temperature lies above gas phase temperature (negative values on horizontal axis). Temperature level in the flame trap section decreases with increasing specific thermal power. This trend is a result of the increasing flow rate of cold gas that intensifies its cooling effect. Within the porous structure section (positive values on horizontal axis), gas temperature (black lines) rises above solid temperature (red lines). After passing a coordinate of maximum value, both gas and solid temperature decrease towards the end of the porous structure with the solid temperature below the gas temperature.

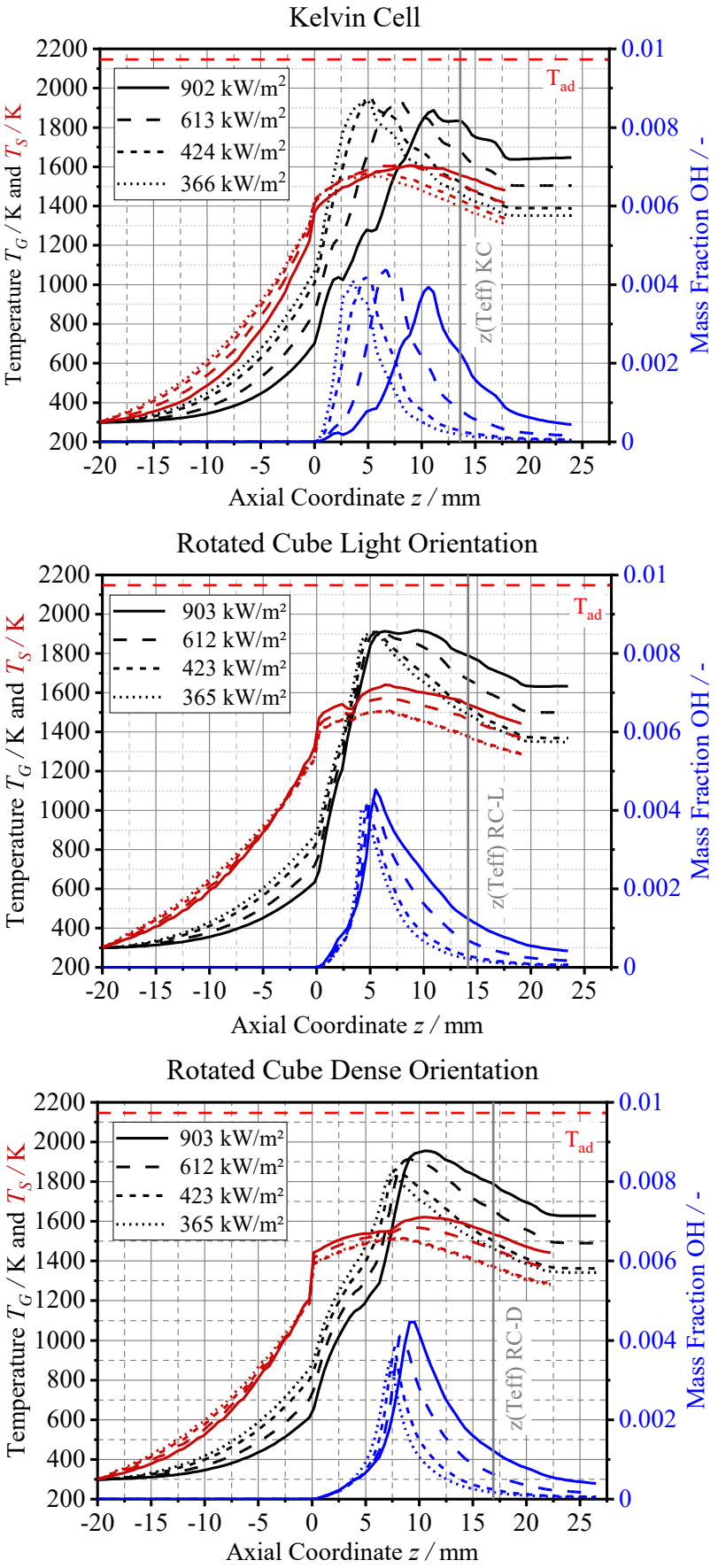

Figure 3. Axial profiles of solid and gas temperature and OH mass fraction for the three structures KC, RC-L and RC-D at four different values of specific thermal power, each.

Temperature level of gaseous and solid phase at the end of the porous structure increase with increasing specific thermal power. This result is in line with Figure 2, where an increased effective radiation temperature is found for increasing specific thermal power. Outlet gas temperature and radiation efficiency are coupled by the balance of enthalpy; with rising gas temperature, a reduced fraction of the combustion energy is available for radiative emission and radiation efficiency decreases. In all cases, OH mass fraction reaches its maximum at approximately the same position as the gas phase temperature and solid temperature; the authors refer to this axial coordinate as the flame position. Position of the effective radiation temperature $z\left(T_{rad}^{eff}\right)$ is defined as downstream axial coordinate at which $T_S = T_{rad}^{eff}$.

For the RC-L structure, flame position is 4-6 mm from the interface of flame trap and porous structure (z = 0) and almost independent of the specific thermal power. Position of effective radiation temperature is located at 14.1 mm, which is 5.4 mm from the structure end for all considered values of specific thermal power. For the RC-D structure, flame position varies between z = 7 mm and z = 10 mm; position of effective radiation temperature is 5.5 mm from the structure end for the range of considered specific thermal power. For the KC setup, flame position ranges from z = 3 mm and z = 11 mm; however, position of effective radiation temperature is independent from specific thermal power and located 4.4 mm from the structure end. The dependence of the flame position on the specific thermal power is a result of the geometrical details in the interaction of flame trap and porous structure. In the KC setup, no duct of the flame trap is axially aligned with a strut of the solid porous structure; the flow from the flame trap forms flow profile comparable to an expanding jet. In RC setups, the axis the flame trap ducts point directly towards a strut of the respective structure. Consequently, the axial momentum of the affected jet is deflected into lateral momentum, which leads to an axial flame position that is independent from the flow rate.

Porous radiant burners rely on the working principle of radiation emission from hot solid surface, but the source of heat is the combustion reaction, which takes place in the gas phase. For better understanding of the gas-solid interaction, heat fluxes and surface area of the interface are evaluated on slices that are oriented normal to the main flow axis. The considered quantities ϕ of interface heat flux and interface area are expressed as volume-specific values with the respective volume given by the cross-sectional area A_S of the slice and finite slice thickness Δz. The specific quantity $\phi_{\Delta z}$ is a function of local values ϕ^*, the discrete value of Δz, and the geometric parameter l_I/A_S that represents the two-dimensional analogue of the specific surface area.

$$\phi_{\Delta z} = \frac{\int_0^{A_I} \phi^* \, dA_I}{A_S \cdot \Delta z} = \frac{1}{\Delta z} \cdot \int_z^{z+\Delta z} \int_0^{\frac{l_I}{A_S}} \phi^* \, d\left(\frac{l_I}{A_S}\right) dz \quad with \quad \lim_{\Delta z \to 0} \phi_{\Delta z} = \int_0^{l_I/A_S} \phi^* \, d\left(\frac{l_I}{A_S}\right) \quad (4)$$

A_I denotes the interface area, A_S the slice area, and l_I the length of the interface line on a two-dimensional slice. The output of Eq. (4, left) depends on the value of slice thickness Δz. In order to eliminate this dependence, Δz has to approach zero which represents the evaluation of two-dimensional slices. However, with the discretized space of a numerical simulation it is convenient to integrate over the interface area A_I and choose discrete values of Δz for the left side of Eq. (4) in such resolution that the averaging does not obscure details of interest. In the present work, the value of Δz is systematically derived for each geometrical setup as 1 % of the solid-associated extent of the domain, resulting in values of 0.38 mm, 0.42 mm and 0.39 mm for the setups KC, RC-D and RC-L, respectively. Axial profiles of the interface-related quantities are presented in Figure 4. Heat fluxes are given as volumetric values determined according to Eq. (4) with net radiant heat flux q_r based on absorption and emission on the solid surface, conductive heat flux q_c based on heat conductivity and temperature gradient on the gas phase side of the interface and total heat flux q_t as sum of q_r and q_c. Specific surface area S_V results from Eq. (4) with ϕ^* set to unity. Surface Temperature T_S is calculated as average value within the slice according to Eq. (4); the gas phase temperature T_G shown in Figure 4 is the mass flow averaged value from Figure 3.

Figure 4 exemplarily presents results from KC at 613 kW/m^2 and both RC setups at 612 kW/m^2; negative z-values on the horizontal axis denote the flame trap section, positive values describe the section of the porous structure. For all cases, q_c values are negative in the flame trap section which

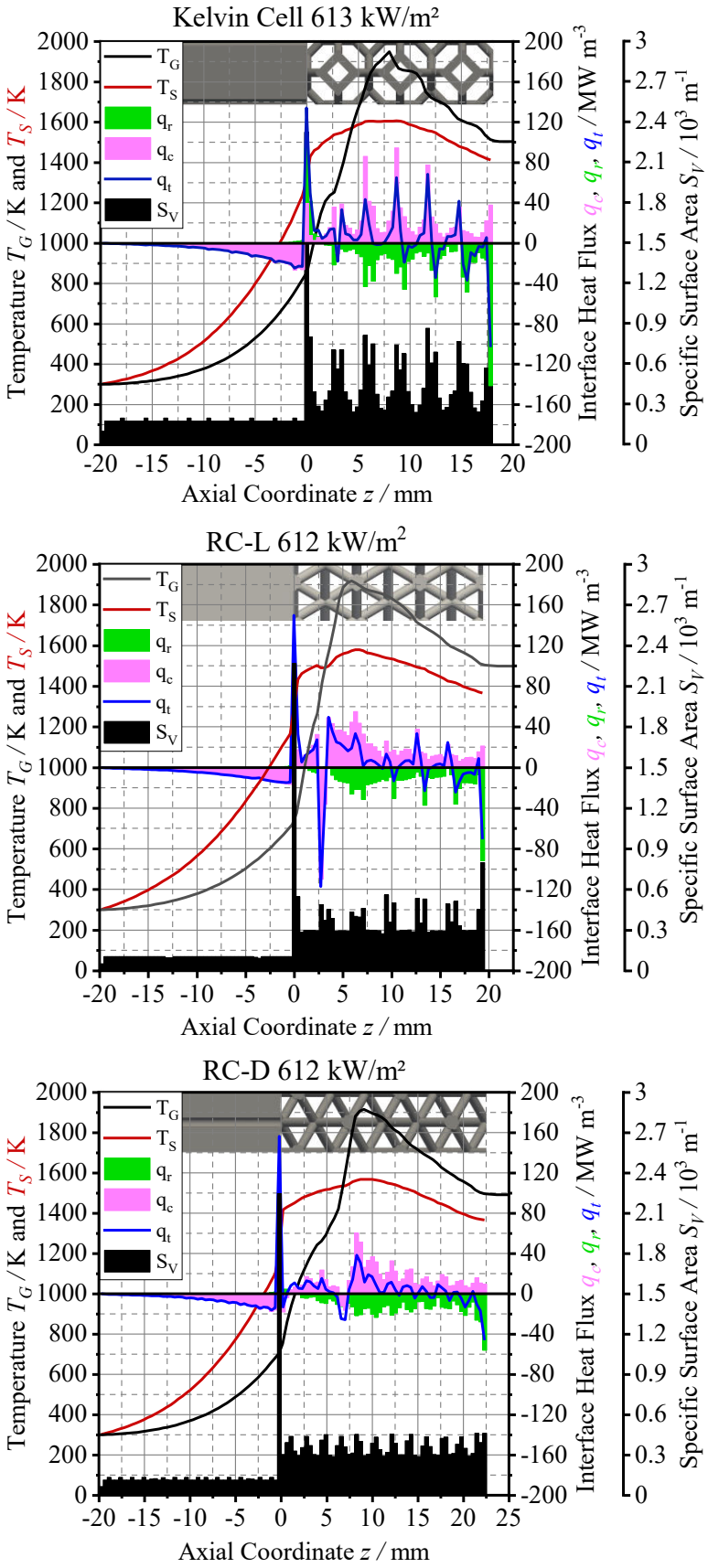

Figure 4. Axial profiles of interface heat fluxes qr, qc, qt, solid surface temperature, mass flow averaged gas phase temperature and specific surface area for the three structures KC, RC-L and RC-D at specific thermal power of 612 kW/m²

means that heat is transferred from the hot solid to the cold gas flow. Total heat flux q_t shows the same trend as q_c, indicating that radiative heat transfer does not play a role inside the narrow channels of the flame trap. In the section of the porous structure, q_r is negative which shows that the structure is net emitting at any z axial coordinate except for the contact zone of flame trap and porous structure. Conductive heat transfer is positive in the section of the porous structure, indicating that heat is transferred from the gas towards the porous structure; exception of this is visible for RC-L at z = 3 mm and RC-D at z = 7 mm. These are the points where cold gas jets from the flame trap hit the hot porous structure.

Specific surface area S_V shows a characteristic pattern that depends on the porous structure. RC-D is only composed of struts that are inclined towards the lateral plane, which is normal to the main flow axis. Values for S_V in the RC-D setup vary periodically with pits at z-coordinates of strut junctions and peaks in between. In the RC-L setup, struts are oriented in the lateral plane in intervals of 3.5 mm, which are recognizable as peaks in the S_V values. The KC setup shows pronounced peaks in intervals of 3 mm; the peaks are associated with struts forming a square that is oriented in the lateral plane. At positions of increased S_V values, peaks in conductive and radiative heat flux area also present. Peaks in q_c are shifted towards the upstream edge of the S_V peak while peaks in q_r are shifted downstream. This finding matches with the mechanisms of heat transfer that scale with the area available. The flow of hot gases hits the strut on the upstream side, causing an increased transfer of heat on the concerned surface. Radiative heat transfer is determined by the temperature distribution on the surfaces that are in radiative exchange. Compared to the upstream side, the downstream side of a strut is facing more surface elements with lower temperature than its local value; consequently, this side of the strut net emits more radiative heat. In the porous structure section, surface temperature (Figure 4) matches with the averaged solid temperature in the respective case of Figure 3; however, in the flame trap section, surface temperature is below the corresponding temperature of the solid phase. This difference indicates the presence of a lateral temperature gradient in the flame trap that is resulting from low heat conductivity and low specific surface area.

The analysis of the gas solid interface demonstrates the impact of available surface area on both, heat transfer from gas to solid and emission of radiative heat. In the downstream section of the porous structure, surface (and solid) temperature T_S is well below the mean gas temperature T_G and conductive heat transfer q_c apparently scales with the temperature difference T_G - T_S and the value of S_V. In the upstream part of the porous structure section, q_c is positive despite the fact that T_S is above T_G, implying heat transfer opposing to the direction that is by the temperature gradient. This impression is caused by the averaging of gas temperature that is dominated by the cold jets near the flame trap. High share of porous structure surface is in contact with recirculating gas that has considerably higher temperature than the average value at this position.

Conclusion

Detailed three-dimensional numerical simulations of two-layer porous radiant burners have been performed, resolving transport of momentum, mass, species and energy on a pore-scale level. A skeletal chemical reaction mechanism was employed for consideration of premixed combustion of methane at equivalence ratio ϕ = 0.91 and radiative heat transfer was accounted for by fvDOM employing grey radiation on 72 discrete ordinates. Three structure setups were considered as periodic representative elements in lateral directions and with full extension of flame trap and porous structure in axial direction. Results show temperature rise of the solid structure and decrease in radiation efficiency with increasing specific thermal power. Both effects are related with increased flue gas temperature at higher specific thermal power of the burner. Orientation of the Rotated Cube structure does not affect radiation efficiency, effective radiation temperature or relative position of the effective radiation temperature. Comparison between Rotated Cube and Kelvin Cell structure demonstrate the positive impact of an increased specific surface area on radiation efficiency. Interface heat fluxes are shown in high axial resolution; contributions of individual heat transfer mechanisms are recognizable.

Acknowledgment

This project has received funding from the European Union's Horizon 2020 research and innovation programme under grant agreement No 768692. The authors acknowledge support by the state of Baden-Württemberg through bwHPC. This work was partially performed on the supercomputer of ForHLR funded by the Ministry of Science, Research and the Arts Baden-Württemberg and by the Federal Ministry of Education and Research.

Literature

[1] Fuessel A., Klemm H., Boettge D., Marschallek F., Adler J., Michaelis A.: *Advancement of Cellular Ceramic Made of Silicon Carbide for Burner Applications*, IOP Conf. Series: Materials Science and Engineering, 18, 1820001, 2011.

[2] Ortona A., D'Angelo C., Gianella S., Gaia.: *Cellular ceramics produced by rapid prototyping and replication*, Materials Letters, 80, 95-98, 2021.

[3] Stelzner B., Keramiotis Ch., Voss S., Founti M.A., Trimis D.: *Analysis of the flame structure for lean methane-air combustion in porous inert media by resolving the hydroxyl radical*, Proceedings of the Combustion Institute 35, 3381-3388, 2015.

[4] Dunnmon J., Sobhani S., Wu M., Fahring R. Ihme M.: *An investigation of internal flame structure in porous media combustion via X-ray Computed Tomography*, Proceedings of the Combustion Institute 000, 1-10, 2016.

[5] Bedoya C., Dinkov I., Habisreuther P., Zarzalis N., Bockhorn H., Parthasarathy P.: *Experimental study, 1D volume-averaged calculations and 3D direct pore level simulations of the flame stabilization in porous inert media at elevated pressure*, Combustion and Flame, 162, 3740-3754, 2015.

[6] Yakovlev I., Zambalov S.: *Three-dimensional pore-scale numerical simulation of methane-air combustion in inert porous media under the conditions of upstream and downstream combustion wave propagation through the media,* Combustion and Flame, 209, 74-98, 2019.

[7] Pelanconi M., Rezaei E., Ortona, A.: *Cellular ceramic architectures produced by hybrid additive manufacturing: a review on the evolution of their design*, Journal of the Ceramic Society of Japan, 128, 595-604, 2020.

[8] EngiCer SA: *Material Data Sheet: SiSiC*, online, http://www.engicer.com/wp-content/uploads/materialdatasheet/EngiCer_Material_Data_Sheet_SiSiC.pdf, accessed 15.06.2021

[9] duotherm Stark Isoliersysteme GmbH&CoKG: *duoForm HT180 (Mullit)*, online, https://duotherm-gmbh.de/downloads/datenblaetter/duobase-datenblaetter.html, accessed 12.10.2019

[10] Bilger R.W., Stårner S.H., Kee R.J.*: On Reduced Mechanisms for Methane-Air Combustion in Nonpremixed Flames*, Combustion and Flame, 80, 135-149, 1990